Chapter 5 The Central Aleutian and Tonga-Kermadec Subduction Zones: Stress, Topography and Geoid in Dynamic Flow Models with a Low Viscosity Wedge.

Abstract

Regional 3-D dynamic models of the central Aleutian subduction zones are used to constrain lateral variations in viscosity in the upper mantle and are compared to previous models for the Tonga-Kermadec subduction zone. Dynamic models include age variations of the lithosphere, crustal thickness variations associated with active and remnant arcs and slab density due to thermal anomalies based on a kinematic model of subduction. Modeling the dynamic topography and the geoid for the central Aleutians requires a low viscosity wedge (LVW) above the slab to decouple the slab-induced flow from the surface and a region of low density material ($\delta\rho = 10$ kg/m^3) coincident with the low viscosity region. The width of the low viscosity region is constrained to the width of the island arc (100 km from the trench) by both dynamic topography and the observation that the overriding plate is not in extension behind the island arc: extension occurs within the overriding plate above the low viscosity region in the wedge. The low viscosity region also changes the orientation of stress in the top of the slab at shallow depths, from down-dip tension to near down-dip compression. Previous models for the Tonga-Kermadec subduction also require a low viscosity, low density ($\delta\rho = 20$ kg/m^3) region within wedge. In these models observations of shallow bathymetry on the overriding plate far from the trench and back arc extension were fit by extending the region of low viscosity beneath the back arc spreading center and the low density region to 300 km west of the back arc spreading center. The LVW also changes the orientation of stress within the slab from down-dip tension to near down-dip compression within the top of the slab at shallow depths transitioning to down-dip compression throughout the slab below 300 km. The low viscosity region changes the flow within the wedge decoupling the slab from wedge and allowing deformation due to viscous flexure of the slab to control the orientation of principal stress directions within the slab. The presence or lack of a low viscosity region may contribute to the observed variability in the combination of stress states within the slab and the overriding plate: down-dip compression or

tension together with either extension or compression of the overriding plate. The difference in the viscosity structure and state of stress in the two regions presented here may reflect differences in the history of subduction including subduction rates, lithosphere age, influences of back-arc spreading, dehydration of the slab and melting within the wedge.

5.1 Introduction

The central Aleutian and the Tonga-Kermadec subduction zones in its present incarnation have been the location of active subduction of the Pacific Plate since 45 Ma. However, several observations show that the state of stress within the subducting and overriding plates in these two subduction zones are very different. The upper plate of the central Aleutian subduction zone consists of old (∼120 Ma) oceanic lithosphere (Bering Sea) [Cooper et al., 1976; Worrall, 1991] between the island arc and continental lithosphere to the northeast and northwest. Beyond the narrow (∼100 km), high topography along the Aleutian Island Arc, the surface of the oceanic crust has an average depth of 8 km below a uniform layer of sediment greater than 4 km thick. The geoid is marked by a narrow low over the trench and high over the back arc and decreases steadily from the back arc over the overriding plate (Figure 5.1) with a total change in height of only 20–30 m. There is no evidence for extension within the overriding plate. Seismicity with the slab extends to only 250–300 km in the central Aleutians shallowing to the west and east. To the east, where the dip of the slab is shallow (25°), the slab appears to be in down-dip tension. However, in the central Aleutian segment, where the slab dip increases to 60°, the slab is in down-dip tension only at very shallow depths (100 km), transitioning to down-dip compression around 150 km [Astiz et al., 1988; Lay et al., 1989].

In contrast, the Tonga-Kermadec subduction zone is characterized by active back arc spreading, a deep trench (6 to 10 km), shallow bathymetry (2.5 km) on the overriding plate, and large positive geoid (40–100 m) and gravity (25–150 mgal) anomalies extending 1000 to 3000 km from the trench on the overriding plate. These observations indicate that the overriding plate is in horizontal extension and may be experiencing regional uplift [Scholl and Herzer, 1992] despite the dense slab beneath which would tend to depress the back arc topography. The maximum depth of the Wadati-Benioff zone increases from ∼300 km in the south to at least 670 km north of 28°S. The stress state within the slab, based on earthquake mechanism, also varies along strike with dominately down-dip compression at all depths in the north and a mix of down-dip compression and tension in the south [Astiz et al., 1988; Lay et al., 1989].

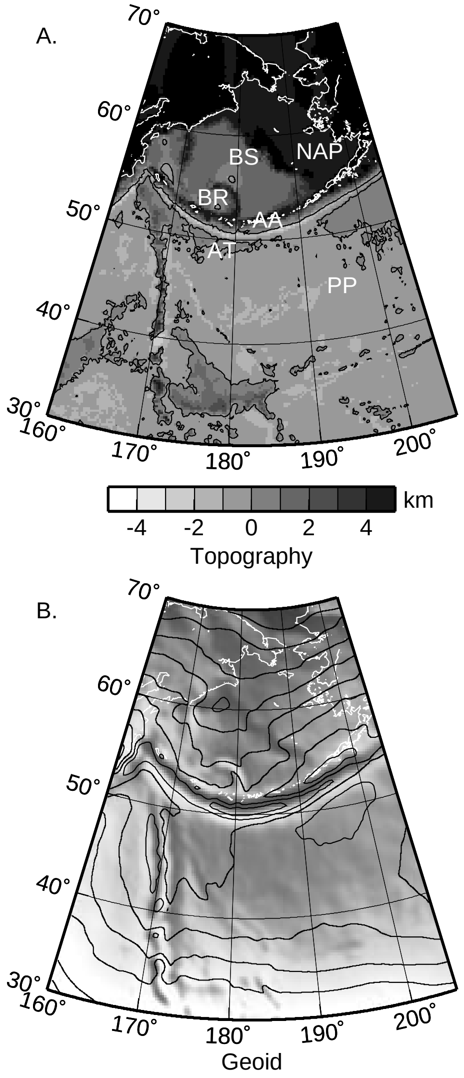

Figure 5.1: Observed bathymetry [GEBCO, 1997] and geoid [Lemoine et al., 1998] for the region of the Aleutian subduction zone. Bathymetric depths have been corrected for sediment thickness [Schroeder, 1984] and shifted up by 5 km for comparison with model results. This places abyssal hill depths on the Pacific plate at ~ 0 km. Contour interval is 10 m (dashed, negative; solid, positive). AT, Aleutian Trench; AA, Aleutian Arc; BR, Bowers Ridge; BS, Bering Sea; NAP, North American Plate; PP, Pacific Plate.

The different state of stress observed in the Aleutians (weak down-dip compression and down-dip tension in the slab with no back arc extension) and Tonga-Kermadec (strong down-dip compression in the slab with back arc extension) illustrates the range of stress states observed in all subduction zones, including every combination of extension and compression within the overriding plate and the slab [Seno and Yamanaka, 1998]. Several models have been proposed to explain the stress state within the overriding plate [McKenzie, 1969; Chase, 1978; Scholz and Campos, 1995] or the slab [Fujita and Kanamori, 1981; Vassiliou et al., 1984; Astiz et al., 1988; Lay et al., 1989; Houseman and Gubbins, 1997]; however, a dynamically self-consistent explanation for the combinations of stress within the subduction zone has not yet been found [Seno and Yamanaka, 1998].

One of the major difficulties in reproducing the wide variation in the combination of stress states has been predicting down-dip compressional stresses at shallow to intermediate (100–300 km) depths in the slab. Vassiliou et al. [1984] showed that the most commonly observed state of stress within the slab, shallow down-dip tension with deeper down-dip compression, is the expected state of stress for a moderately strong slab sinking into the mantle and meeting resistance due to an increase in viscosity near 670 km depth. Houseman and Gubbins [1997] demonstrated that down-dip compression within the slab is expected if a strong slab is decoupled from the surrounding asthenosphere, allowing bending stresses within the slab due to viscous flexure to control the deformation of the slab. However, none of the approaches used in these models could simultaneously address the state of stress within the overriding plate, either because the overriding plate was modeled as a rigid plate [e. g. Vassiliou et al., 1984] or the slab was explicitly decoupled from the surrounding asthenosphere and the overriding plate [e. g. Houseman and Gubbins, 1997].

Most previous models used to explain the causes of back arc spreading have relied on force balance calculations in which the influence of slab induced flow on the overriding plate is parameterized in terms of coupling within the lithosphere and ignores the forces on the base of the lithosphere caused by flow within the wedge. Numerical models of instantaneous Stokes flow demonstrate that the slab beneath the overriding plate drags the overlying wedge down and towards the slab and therefore transmits large stresses to the overriding plate [Sleep, 1975; Zhong and Gurnis, 1994; Zhong et al., 1998]. The flow induced by the slab in the wedge pulls down on the overlying asthenosphere and lithosphere putting the overriding plate into compression and creating a broad (200–500 km), deep (3–4 km) basin in the back arc region. Sleep [1975] found that in order to match the topography and gravity signal on the overriding plate in 2-D models of the Central Aleutian subduction zone, it was necessary to include a local region of low viscosity within the wedge beneath the island arc. However, a good match to both the gravity and topography was not found, in part because the plate boundary was incorporated as a shear zone and a very dense slab was needed to match the trench depth. Zhong and Gurnis [1994] and Zhong et al. [1998] showed that trench morphology and depth could be predicted without increasing the slab density by including a fault along the subduction boundary, but did not explore the role of localized regions of low viscosity.

Here we present 3-D instantaneous, Stokes flow models for the Central Aleutian subduction zone. The models include a faulted plate boundary, radial- and temperature-dependent viscosity, and localized regions of low viscosity and/or low density (independent of temperature) within the wedge above the slab. We use observations of dynamic topography, the geoid, and stress within the slab and overriding plate to constrain the viscosity and buoyancy structure within the subduction zone. We find that it is necessary to include a small, low viscosity and low density region above the slab to simultaneously match both the dynamic topography and the geoid and in doing so are still able to match the state of stress within the slab and overriding plate. Similar modeling was previously carried out for the Tonga-Kermadec subduction zone [Chapter 3 and 4], in which it was found that a large low viscosity, low density region was required to fit the observations. We will first present the new models for the Central Aleutians. We will then summarize the previous results for the Tonga-Kermadec subduction zone and show that the presence of a low viscosity region within the wedge provides a dynamically self-consistent explanation for several geophysical and geochemical observations characterizing both subduction zones.

5.2 Numerical Method

We investigate the influence of local variations in viscosity and buoyancy on the dynamics of a subduction zone using a finite element model for instantaneous viscous flow. Flow in the mantle is governed by the equations for conservation of mass and momentum. Assuming that inertial forces are negligible and applying the Boussinesq approximation, the equations of motion for flow caused by internal buoyancy anomalies are

$$\nabla \cdot \mathbf{u} = 0 \tag{5.1}$$

and

$$\nabla \cdot \sigma + \mathbf{f} = 0 \tag{5.2}$$

where $\mathbf{u}$, $\mathbf{f}$ and σ are the flow velocity, the body force and stress tensor, respectively. The body force includes density anomalies due to temperature T,

$$f_i = \rho_o \alpha (T - T_o) g \delta_{ir} \tag{5.3}$$

where ρ_o is the reference density, T_o is reference temperature, g is the gravitational acceleration, α is the coefficient of thermal expansion and δ_{ij} is Kronecker delta. Inferred density variations due to composition are included in terms of equivalent temperature. The equations are solved with a primitive variable formulation using **CitcomT** [Chapter 4] a 3-D, spherical geometry finite element code based on the Cartesian code **Citcom** [Moresi and Solomatov, 1995; Moresi and Gurnis, 1996; Zhong et al., 1998]. The code has been tested extensively and validated with analytic solutions for flow and topography with large radial and lateral variations in viscosity [Chapter 4].

The model domain extends from the surface to the core-mantle boundary, 45° in longitude (160°-200°) and 40° in latitude (30°N–70°N). The top and bottom surfaces have free-slip, isothermal boundary conditions. The side-walls defined as planes of equal longitude or latitude have reflecting boundary conditions (no shear stress). Element size ranges from 2.5 km within the wedge, slab and upper 200 km of the model, to 100 km away from the trench and surface. A fault along the subduction zone boundary is modeled with boundary conditions requiring continuous normal stress, but allowing discontinuous tangential stresses on the fault interface [Zhong and Gurnis, 1994; Zhong et al., 1998]. While the true dip of the fault at the surface ranges from 10°–30°, due to numerical constraints on distortion of the rectangular elements used in the model, the maximum dip of the fault within the top 10 km is 30°.

Flow is driven by internal buoyancy sources due to temperature, including the

Table 5.1: Model Parameters

Variable Name		**Value**
Reference density	ρ_o	3300 kg/m^3
Temperature difference from top to bottom surface	ΔT	1500 K
Thermal diffusivity	κ	1$\times$10^6 m^2/s
Coefficient of thermal expansion	α	2$\times$10^{-5} K^{-1}
Earth radius	R	6371.137 km
Gravitational acceleration	g	10 m/s^2
Reference viscosity	η_o	3$\times$10^{20} Pa s
Rayleigh number	Ra	8.53$\times$10^8

slab and variations in lithosphere age, and chemical heterogeneities, including crustal thickness variations within the island arc and continents and variations in mineralogy and melt content in the wedge above the slab. The thermal structure of the slab is derived from a kinematic model of flow constrained to follow the location of the slab delineated by seismicity from the surface to the maximum depth of seismicity (300 km). The starting temperature for the kinematic model is defined by a half-space cooling model for each plate based on its estimated age at the beginning of subduction [Müller et al., 1997; Cooper et al., 1976; Worrall, 1991]. Figure 5.2A shows the ages based on well recognized magnetic anomalies [Müller et al., 1997]. In Figure 5.2B, the ages for the overriding plate are extrapolated based on possible spreading anomalies on the seafloor in Bering Sea [Cooper et al., 1976; Worrall, 1991]. In areas where the age is not known we assign an age of 80 Ma. This value is also assigned to a 500 km wide border along the edges of the model domain to avoid offsets in topography across the model boundary in the geoid calculation. The flow field consists of a corner flow above and below the top surface of the slab (including the subducting lithospheric plate) and a fixed overriding plate. The maximum density anomaly within the slab is ∼66 kg/m^3 assuming the values listed in Table 5.1. Crustal density anomalies are assumed to be 500 kg/m^3.

Density variations due to melting processes within the wedge are not well known. However, low density regions with density differences up to 20 kg/m^3 due to large melt

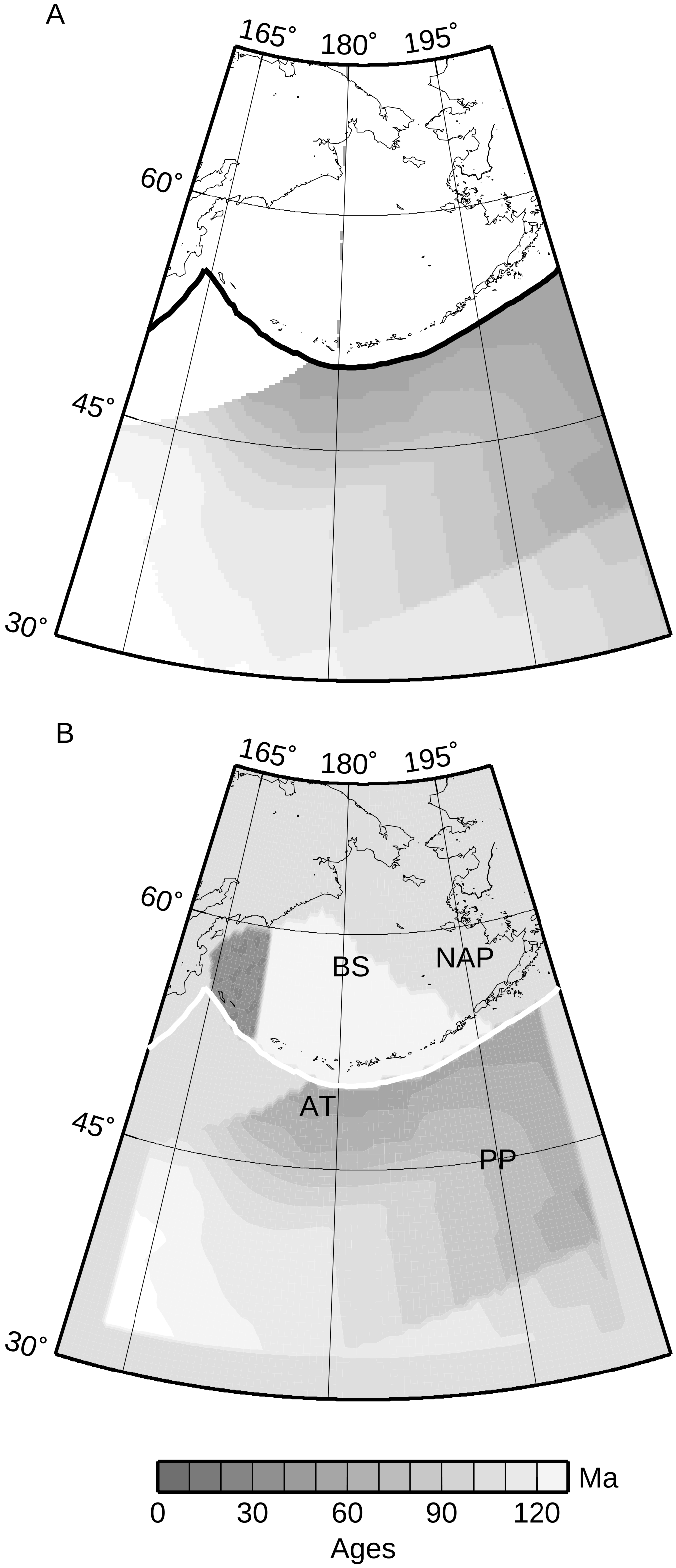

Figure 5.2: **A.** Age of the seafloor within the model domain known from well recognized magnetic anomalies [Müller et al., 1997]. **B.** Age of the seafloor possible magnetic anomalies on the overriding plate [Cooper et al., 1976; Worrall, 1991]. White regions indicate continental crust. Location labels are the same as Figure 5.1.

fraction within and at the base of the crust beneath the island arc are not unreasonable [Rigden et al., 1984]. Low density regions may occur deeper in the wedge due to high degrees of melting of peridotite [Stolper and Newman, 1994] expected due to high concentrations of water within the wedge derived from dehydration reactions within the subducting slab [Tatsumi et al., 1983; Morris et al., 1990; Schmidt and Poli, 1998]. Less garnet forms within the garnet stability field ($P > 30$ kbar) in highly depleted peridotite due to the loss of Al_2O_3, leading to a decrease in density, compared to fertile peridotite, of up to 50 kg/m^3 (for 30 wt% melting) (P. Asimow, personal communication).

The background viscosity structure consists of four layers: lithosphere (0–100 km), asthenosphere (100–410 km), transition zone (410–670 km) and lower mantle (670–2890 km). The viscosity of each layer is defined with respect to a reference viscosity η_o. We choose to have the reference viscosity coincide with the viscosity in the asthenosphere with a value of 3×10^{20} Pa s. The temperature dependence of the non-dimensional viscosity in each layer is given by

$$\eta'(r', T') = \eta^*(r, \phi, \theta) \exp\left(\frac{c_1}{T' + c_2} - \frac{c_1}{1 + c_2}\right) \tag{5.4}$$

where the constants c_1, c_2 and $\eta^*(r, \theta, \phi)$ can differ in each layer. For the background viscosity structure $\eta^*(r, \theta, \phi)$ has a value of 100, 1, 10 and 100 in the lithosphere, asthenosphere, transition zone and lower mantle, respectively, and the maximum viscosity of the slab at all depths is $100 \times \eta_o$.

Lateral variations in viscosity not due to temperature are included by setting c_1 and c_2 to zero and η^* to the desired viscosity. A low viscosity region within the wedge (LVW) may be caused by high concentrations of water [Mei, 1999; Karato, in press] or melt at shallow depths [Hirth and Kohlstedt, 1995, 1996; Phipps-Morgan, 1997; Kelemen et al., 1997]. Seismic observations in several subduction zones show regions of low seismic velocity within the wedge extending from the base of the crust to greater than 200 km [Hasegawa et al., 1991; Zhao et al., 1992; Roth et al., 2000]. These deep seismic anomalies may be caused by the presence of water [Karato, in press]. In the Central Aleutians, seismic refraction data are consistent with a region of slow seismic velocity in a narrow region parallel to the slab from beneath the island arc to depths of 100 km [Grow, 1973]. Seismic tomography in the Shumagin region of the arc reveal slow seismic velocity regions within the crust beneath the island arc and extending into the wedge [Abers, 1994].

Dynamic topography, geoid height and stress orientations are compared with observations to assess the success of each viscosity and buoyancy model. Because the overriding plate within the Bering Sea is covered with thick sediments (> 4 km) it is necessary to correct the observed topography for the sediment load. The sediments could be incorporated in the dynamic model as an effective density anomaly on the overriding plate. However, since these density anomalies do not contribute to uncompensated topography (i. e., due to change in flow) and it is straightforward to correct for the influence of the sediments on topography, we calculate a residual topography for comparison with the predicted dynamic topography from the models. We use the bathymetric data base from ship track data measurements [GEBCO, 1997] for the observed topography. We then subtract the thickness of the sediments [Laske and Masters, 1997] and, assuming local isostasy, correct for the change in depth of the seafloor due to the weight of the sediments [Schroeder, 1984]. Using this approach, dynamic topography away from the active subduction zone margin is approximately zero (Figure 5.3).

We calculate the predicted geoid using spherical harmonic functions and include contributions from dynamic topography on the surface and core-mantle boundary and density anomalies within the mantle, which implicitly assumes that there are no density anomalies outside the model domain. This means that topography outside the model is zero and any topography on the top or bottom surface of the model along these boundaries creates a step in topography across the side boundaries, leading to large short wavelength noise in the predicted geoid. To minimize any offset in topography across the model boundaries, we taper crustal density anomalies to zero 500 km from the domain boundaries, set the age of the lithosphere along the boundary to 100 Ma and shift the predicted topography everywhere by the mean value along the edge of the domain.

The trench depth in the models is much larger than observed due to a stress

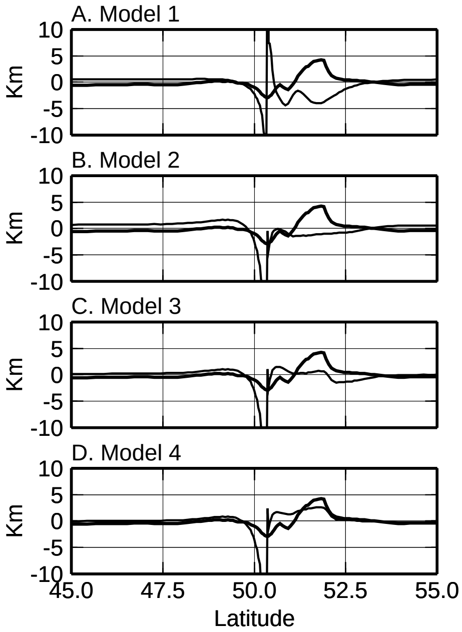

Figure 5.3: Comparison of residual topography (thick line, see text for calculation of residual topography) and model (thin line) dynamic topography for north-south cross sections at 182^o. **A.** Model 1, radial- and temperature-dependent viscosity. **B.** Model 2, includes a low viscosity region in the wedge (LVW) and a narrow shear zone along the plate boundary fault. **C.** Model 3, includes crustal thickness variations for the active island arc, Bowers Ridge and continental regions. **D.** Model 4, includes low density region coincident with the LVW ($\Delta\rho$=10 kg/m^3).

singularity at the the fault tip that increases with decreasing element size. Since we use small elements along the top surface of the slab to accurately model sharp viscosity boundaries, the stress singularity in the models leads to trench depths of greater than 15 km. In calculating the contribution to the geoid due to topography we limit the maximum depth of the trench to 5 km. The stress singularity also creates a large peak in topography in the fore arc on the overriding plate. Including a weak zone above the fault (20 km wide perpendicular to the fault) simulating the highly faulted accretionary wedge in the fore arc reduces this peak to 1–2 km.

The observed geoid within the model domain includes large long wavelength signal from processes not included in the subduction zone models (Figure 5.1). Therefore, we compare the observed geoid to the predicted geoid using a spatio-spectral localization method [Simons, 1996]. This method allows us to calculate the position and wavelength (or harmonic degree) dependent correlation between the observed and predicted geoid. We then limit our analysis to wavelengths smaller than half the

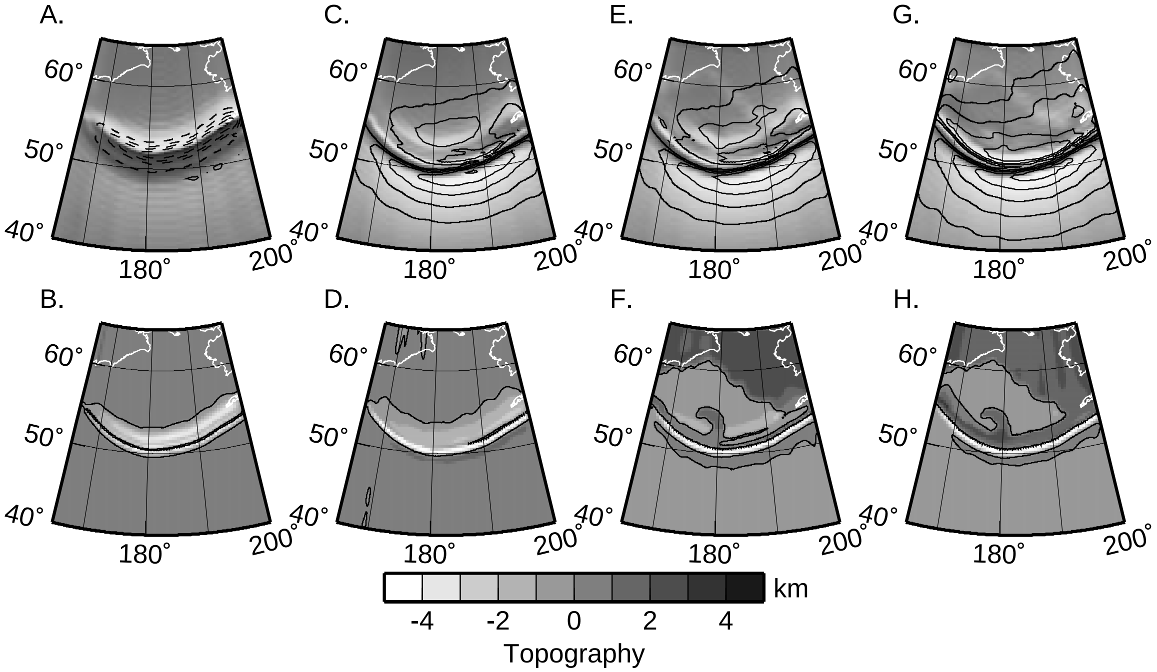

Figure 5.4: **A.** Predicted geoid and **B.** dynamic topography for model 1. Contour interval for the geoid is 10 m (dashed, negative; solid, positive). Only part of the domain is shown here: 5^o is omitted on the east, west and north boundaries since age and crustal variation are not included along the edge of the model domain and 10^o is omitted on the south boundary since there is no variation in the topography or geoid in this region of the models. **C, D.** Model 2. **E, F.** Model 3. **G, H.** Model 4.

size of the domain (2000 km) and larger than twice the size of the largest element (200 km). Using this method we can limit the analysis to signal within the region of the model caused by processes included in the model.

5.3 3-D Model Results for the Central Aleutians

The observed topography across the Central Aleutian subduction zone includes a small forebulge (200–300 m), a small (2.5 km deep) narrow (50 km) trench, a fore arc high immediately adjacent to the trench and a narrow region of high topography (4 km) along the island arc. Model 1 which includes only radial- and temperature-dependent viscosity predicts a large topographic basin over the island arc region (Figure 5.3A and 5.4B). The abrupt change in dip of the fault from 30° to 60° at a depth of 50 km focuses stress above it creating the small bump within the basin. The overriding plate is in compression in a 300 km wide region above the slab. Further from the slab the overriding plate is in tension, but this is due to boundary conditions on the flow with zero horizontal velocity at the model boundaries. The slab is in down-dip or vertical tension at all depths (0–250 km) except for the leading edge of the slab (deepest 25–50 km) which is in down-dip compression. The large basin and compressional stress in the overriding plate are caused by coupling of the downward flow caused by the sinking slab to the overriding plate.

The broad, deep basin creates a large geoid low above the back arc and the long wavelength geoid is almost flat across the model domain (Figure 5.4A and 5.5A,B). The localized correlation between the observed and predicted geoid has a large negative correlation directly beneath the trench and back arc region at all wavelengths. Beneath the forebulge on the subducting plate, positive correlations at short wavelengths (< 500 km) indicate that this region of the model agrees with the observed geoid, despite the large misfit over the trench.

In order to decrease the depth of the basin on the overriding plate, in model 2 we include a low viscosity region parallel to the slab. The low viscosity region is 100 km wide from the top surface of slab to the island-arc region and extending from 20 km depth to 150 km. A narrow shear zone (20 km wide) is also included above the fault from the surface to 20 km depth. The viscosity within the LVW is $0.1 \times \eta_o$ and the viscosity of the shear zone is η_o. The LVW has a dramatic effect on the topography of the overriding plate, almost completely eliminating the basin (Figure 5.3B and 5.4D). The thick, strong lithosphere of the overriding plate is strongly coupled to the slab induced flow within mantle requiring that the width of the LVW is at least as wide as the basin in Model 1 to decrease the basin depth across its entire width [Chapter 3] . A narrow LVW would allow the basin depth to increase beyond the edge of the LVW furthest from the slab. A wider LVW would also decrease the basin depth; however, we found that a wider LVW produced small, short wavelength positive topography beyond the island arc region which is not observed. The overriding plate remains in horizontal compression above the low viscosity region, while the orientation of stress within the top of the slab (25 km thick), deeper than 100 km, is no longer in down-dip tension. Instead the principal compression directions are aligned with a dip approximately 20° less than the local dip of the slab, rotating into down-dip

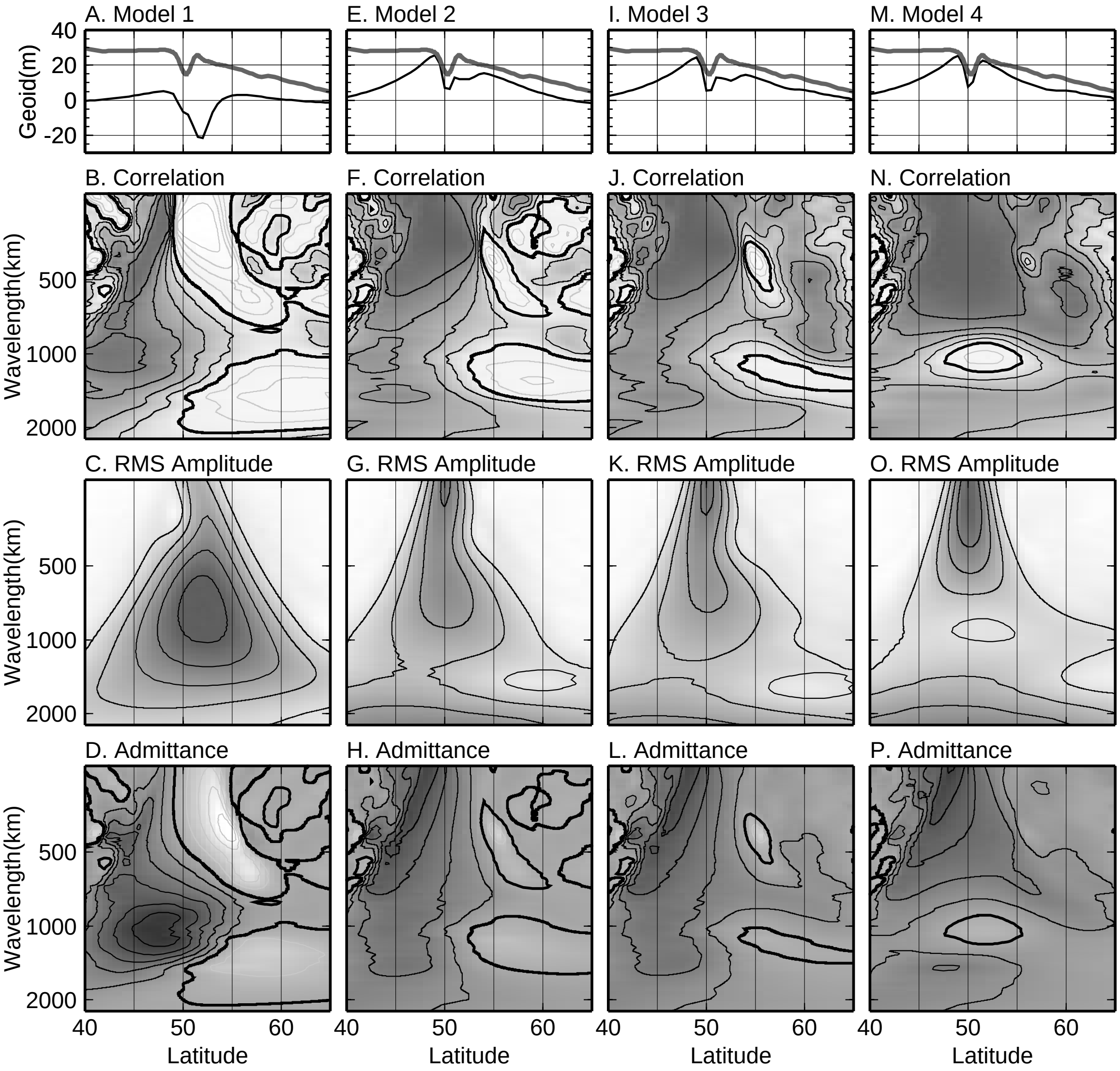

Figure 5.5: Geoid localization for north-south cross section at 182^o. **A.** Comparison or observed (thick line) and predicted (thin line) geoid for model 1. An north-south linear ramp is removed from the profiles for comparison **B.** Position and wavelength dependent correlation between observed and predicted geoid. Positive values are indicated by dark regions and black contours. Negative values are indicated by light regions and gray contours. Zero contour is marked by the thick black contour. Contour interval is 0.2. **C.** RMS amplitude of model geoid. Contour interval is 1. **D.** Admittance. Positive values are indicated by dark regions and black contours. Negative values are indicated by light regions and gray contours. Zero contour is marked by the thick black contour. Contour interval is 0.5. **E–H.** Model 2. **I–L.** Model 3. **M–P.** Model 4.

compression between 200 and 300 km. The interior and bottom of the slab remain in down-dip compression.

By reducing the size of the basin, the large geoid low over the back arc disappears and is replaced by a small, narrow geoid low directly over the trench with only a flattening out of the geoid over the island arc region (Figure 5.4C and 5.5C,D). A long wavelength geoid high, with a peak amplitude of 25 m, now dominates the geoid signal over the subduction zone. The higher correlations (> 0.8) obtained from the localization analysis confirm the improved agreement with the observations at wavelengths of 500 km, except beneath the island arc where the geoid is less than observed. Although the slope of the geoid over the region north of the island arc is similar to observed, the correlations show that at both short and intermediate wavelengths this part of the geoid is still not well modeled. In the island arc region the mismatch at short wavelengths is probably caused by missing crustal density anomalies. North of the back arc a small change in the slope of the observed geoid at 58°N coincides with the edge of the continental shelf in the Bering Sea.

To improve the fit of the observed topography at short wavelengths, in model 3 we include density anomalies due to crustal thickness variations within the island arc, Bowers Ridge (18 km) and the continental regions (20 km). Including the continental crust improves the fit to both the observed topography (Figure 5.3C and 5.4F) and the geoid (Figure 5.4E and 5.5E,F), although a larger thickness is probably needed: the predicted height of the continents is shallow by about 2 km. The crustal anomalies within the island arc create some positive topography, but the amplitude is too small and a small basin is present behind the island arc where the observed topography increases approaching the far side of the island arc. No observations indicate that other crustal anomalies should exist behind the island arc and the long wavelength character of the topography in the region suggests that it is caused by a deeper source of buoyancy. The stress within the slab and overriding plate are unchanged from model 2.

In model 4 we reduce the density within the LVW by 10 kg/m^3 compared to the surrounding asthenosphere and lithosphere. We did not vary the size of the low density region under the assumption that the low viscosity and low density are caused by the same processes. The density anomaly within the LVW was adjusted to fit the slope and amplitude of the topography behind the island arc. Including the low density region improves the fit to observed height of the island arc. The height of the fore-arc region is too high, but this may be due to crustal density anomalies in the model extending into the fore arc region. The fore arc is an accretionary prism made up of pieces of oceanic crust sliced off the subducting lithosphere [Grow, 1973] and therefore may not have density as low as would be expected if the accretionary prism were composed of only sediments scraped off the subducting crust.

The match to the observed geoid improves significantly. The cross section of the geoid (Figure 5.5G) shows a good match to the short wavelength low over the trench. The short wavelength high over the back arc is slightly broader than observed and this probably reflects the misfit in the topography over the fore arc. The region of positive correlation now spans the entire width of the subduction zone with values over 0.95 for wavelengths less than about 700 km. The region of low or negative correlation at wavelengths of 1000 km highlights the difference in slope of the observed and predicted geoid at these wavelengths. While this can not be visually compared on the subducting plate side, above the overriding plate the slope of the predicted geoid increases more rapidly approaching the trench, than the observed geoid. This difference in slope and negative correlation at intermediate wavelengths may indicate that the density of the slab in these models is too large.

Low density within the wedge does not change the orientation of stress within the slab compared with model 2 or model 3; however, the orientation of stress within the overriding plate now includes a region of horizontal extension, limited to the region directly above the LVW, beneath the island arc, with horizontal compression in the fore arc region. The magnitude of extension decreases at the boundary of the LVW before reaching the region where there is extension controlled by the boundary conditions.

5.4 Discussion and Conclusions

The results for the Central Aleutian model 4 are compared to previous results for the Tonga-Kermadec subduction zone in Figure 5.6 [Chapter 4]. A low viscosity, low density region within the wedge is also needed to match observations of topography, geoid and stress in the Tonga-Kermadec models. The complex history of the

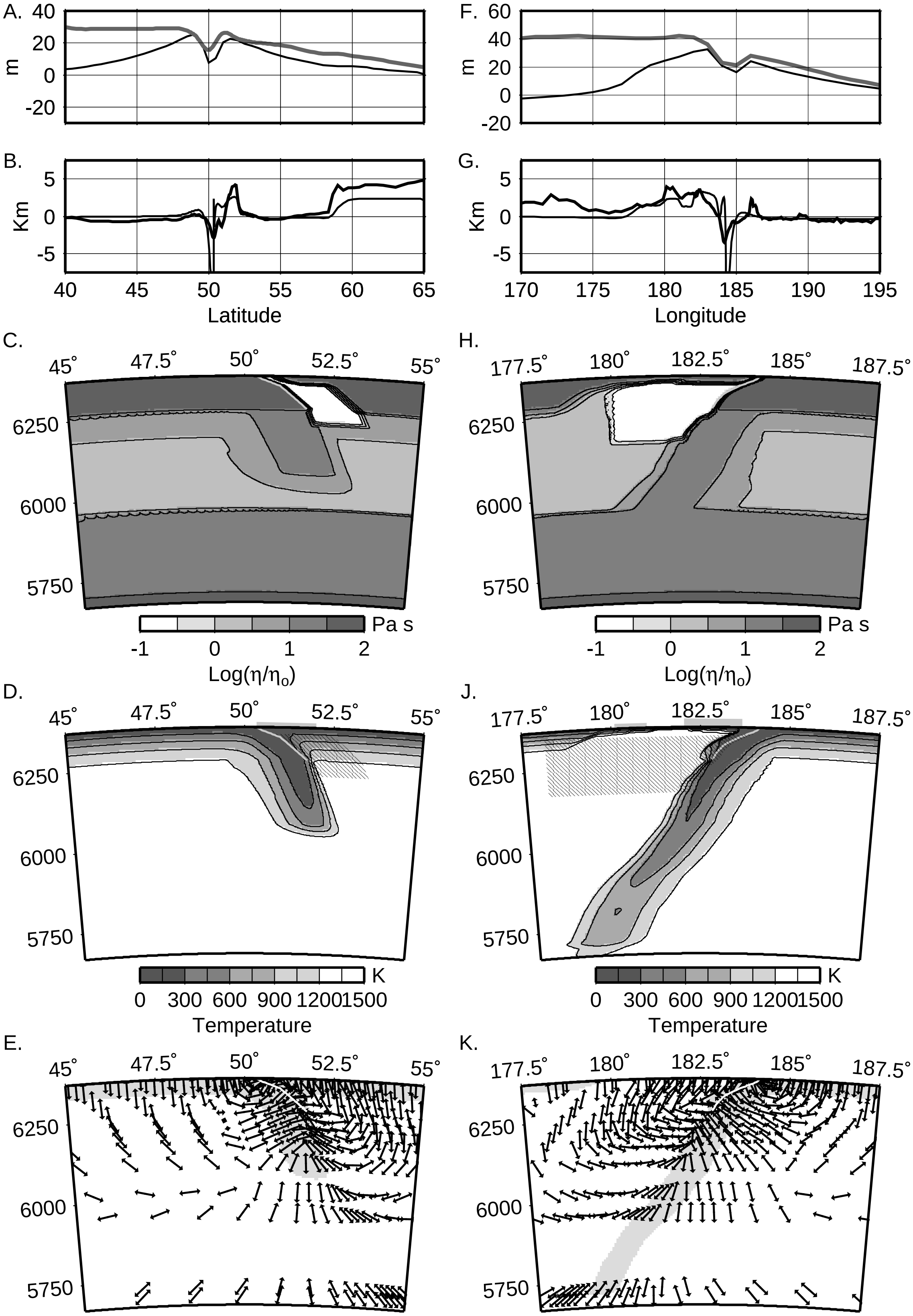

Figure 5.6: See caption next page

subduction zone including several episodes of back arc spreading and slab roll-back and the presence of other slabs within the model domain, but not included in the flow models, make it more difficult to match the geoid and topography more than 500–1000 km from the trench. However, shallow bathymetry extending more than 1500 km from the trench on the overriding plate and active back arc extension require a much broader low viscosity region extending beyond the island arc and back arc spreading center and broader low density region extending at least 800 km from the trench, in contrast with the results for the Central Aleutians. The low viscosity and low density regions extend from 20 km to 200 km in depth and the density anomaly is 20 kg/m^3. In addition, the density anomaly due to the slab for the Tonga-Kermadec model was reduced by a factor of two in order to match the short intermediate wavelength amplitude of the geoid above the trench. A denser slab lead to a large misfit with the amplitude of the geoid above the trench 30–40 m greater than observed, but no change in the density of the slab is needed for the models of the Aleutians.

The orientation of stress within the shallow (100–200 km) portion of the top of the slab is neither down-dip compression or tension. Instead the principal compression axis are oriented 20–30° shallower than the down-dip direction ($\sim$ 60–80°), rotating to down-dip compression throughout the slab below 200 km. The bottom of the slab at shallow to intermediate depths (100–300 km) is primarily in down-dip tension, although the principal tension axis are also rotated 10–20° steeper than the down-dip direction in the shallow (100–200 km) portion of the slab. In 2-D models across the Tonga-Kermadec slab at 28°S with the same viscosity and buoyancy structure,

Figure 5.6: Comparison of central Aleutians (CA), **A-E.** and Tonga-Kermadec (TK), **F-J.** subduction zone models. **A, F.** Cross section of observed (thick line) and predicted (thin line) geoid at 182^o (CA) and 28^{o}S (TK). **B, G.** Cross sections of observed (thick line) and predicted (thin line) topography. For CA, the observed topography is corrected for the sediment load in the Bering Sea (see text). **C, H.** Cross sections of viscosity structure including an LVW and shear zone above the fault. **D, I.** Temperature structure including the location of crustal density anomalies (gray boxes) and wedge buoyancy (hatched region). Contour interval is 300 K. **E, J.** Principal compressive stress directions projected into the plane of the cross section. In profiles the observed geoid or topography is shifted to align with the predicted topography or geoid at the northern (CA) or eastern (TK) boundary of the model.

down-dip compression occurred in the top of the slab at all depths, indicating that the 3-D geometry of the slab is influencing the orientation of stress. In particular we find that the principal tension directions have an along strike component, possibly caused by the change in depth of the slab along strike. None of the 3-D models for the Aleutians have a similar along axis component of the principal stress axis, but the slab geometry is more uniform along strike in the Central Aleutians than it is in the Tonga-Kermadec region.

The difference in size and density of the low viscosity region in the wedge for the Central Aleutians and Tonga-Kermadec is consistent with the difference in the observed stress state and the influence change in flow observed in the instantaneous models could have on the evolution of the overriding and subducting plate:

1. The presence of a large LVW could lead to extension of the overriding plate contributing to stresses causing back arc spreading. The region of extension in models is limited to the width of the LVW.

2. A LVW could contribute to slab rollback by decoupling the slab from the wedge removing this source of support of the negative buoyancy of the slab.

3. Flow within the wedge increases in magnitude and includes an upward component of flow which could draw the residue of melting from beneath the back arc beneath the island arc leading to more extensive depletion and larger density anomalies (lower total density).

4. Decoupling of the slab due to the lower viscosity could lead to slab rollback which abandons low density material in the location of previous island arcs and back arc spreading regions.

These processes depend on a large amount of water added to the wedge being transported several hundreds of kilometers from the slab, lowering the viscosity of the wedge and facilitating higher degrees of melting than would otherwise occur beneath the island arc and back arc spreading center.

The processes associated with water percolating into wedge from the slab and their affect on rheology and buoyancy in the wedge provides a self consistent model for the complex set of observations at both the Central Aleutians and Tonga-Kermadec subduction zones. However, one question which remains is what controls the difference in size of the LVW in these two subduction zones. The large low viscosity region in the Tonga-Kermadec models suggests that the low viscosity region may need to reach a critical size in order to modify flow sufficiently to cause back arc spreading and slab rollback. This dependence on the size of the low viscosity region may contribute to the observed episodic nature of these processes in many subduction zones and could create a positive feedback due to the additional change in buoyancy. If the LVW is caused by water from the slab, then the size and depth extent of the wedge will depend on both the amount of water leaving the slab, how deep the water can be carried down by the slab and how water is transported away from the slab.

Schmidt and Poli [1998] showed that dehydration of the slab may be a continuous process beginning at a depth of 50 km within the subduction zone and extending to depths greater than 300 km within the subducted slab. The maximum depth to which dehydration extends depends on the temperature along the top portion of the slab. Warmer slabs will dehydrate at shallower depths, while older slabs may carry water into the transition zone. Therefore, the difference in the depth extent and size of the LVW in the Central Aleutian and Tonga-Kermadec models may be controlled in part by the age of the subducting plate. In the Central Aleutians the age of subducting plate is currently ∼55 Ma, while in the Tonga-Kermadec subduction zone the age of the plate is between ∼80 and ∼120 Ma [Chapter 1].

The presence of a low viscosity region creates a complex state of stress within the slab that differs significantly from the state of stress predicted by models without a weak wedge. In models with a uniform viscosity asthenosphere, flow in the wedge creates a strong component of down-dip tension which dominates the state of stress in the shallow portion of the slab [Vassiliou et al., 1984],[Chapter 4]. The presence of a low viscosity region changes the flow within the wedge, decoupling the slab from the surrounding flow and allowing deformation due to viscous flexure of the slab to control the orientation of principal stress directions within the slab. In both the Central Aleutian and Tonga-Kermadec models, the LVW creates a region of down-dip or near down-dip compression within the top 25–50 km of the slab between

100–300 km depth. In Tonga-Kermadec, where the slab is in contact with the higher viscosity lower mantle, this region widens to fill the entire width of the slab deeper than about 300 km. Based on these results and previous 2-D models [Chapter 4], the large variability in combinations of stress states within the slab and overriding plate may be explained by the presence or lack of a low viscosity wedge, whether the slab is in contact with a high viscosity lower mantle and the relative strength of the slab. An LVW may be present in subduction zones with a slab in either down-dip compression or tension depending on the internal deformation of the slab. If the slab is strong, but weaker than the lower mantle, the slab will be in down-dip or near down-dip compression at all depths. However, if the slab is stronger than the lower mantle or is not in contact with the lower mantle, then the slab will be down-dip tension or only have a narrow region of near down-dip compression. In subduction zones without a LVW, the slab will be in down-dip tension at shallow depths transitioning to down-dip compression if the slab is in contact with a stronger lower mantle. At the same time the stress state of the overriding plate will depend on the width of the LVW perpendicular to the slab, with wider low viscosity regions causing back arc extension.

Three-dimensional models presented for the Central Aleutian subduction zone demonstrate that a low viscosity and low density region in the wedge above the slab is necessary to match observations of topography, geoid and stress within the slab and overriding plate. The LVW acts to decouple flow induced stresses to the overriding plate reducing the size and depth of the basin on the overriding plate in models without a LVW. The lack of observed extension beyond the island arc region in the Central Aleutians constrains the width of the LVW perpendicular to the slab to the width of the island arc. Crustal density anomalies are needed to match the observed short wavelength ($<$ 100–200 km) topography coincident with the island arc and are probably associated with long term emplacement of magma in the lower crust and beneath active volcanos in the upper crust. Agreement between the observed and predicted topography and geoid at intermediate wavelengths (500–1000 km) is improved by also including a region of lower density coincident with the LVW consistent with the hypothesis that the viscosity and density within the wedge are altered by water derived from the slab and subsequent depletion of the wedge material due to high degrees of melting. Previous modeling of the Tonga-Kermadec subduction zone also found that a low viscosity, low density region in the wedge is necessary to match observations of topography, geoid and stress. The low viscosity and low density regions extend deeper and further from the slab than these regions in the Central Aleutians models possibly reflecting the long history of slab rollback and back arc spreading in that region.

Including a low viscosity and low density region in subduction zone models provides an explanation for several geophysical observations and is consistent with seismic observations and the geochemical processes occurring within the subduction zone. The instantaneous models used here do not enable us to test how the presence of a low viscosity region will affect the evolution of the slab, the wedge and the overriding plate in time. Of particular importance is whether a LVW is sufficient to cause back arc spreading and slab rollback or whether additional far field stresses are needed and why the slab density based on thermal models for the Tonga-Kermadec model is too high by a factor of two. It is unclear what mechanism could decrease the effective density of the slab by this amount, and further modeling is needed to confirm this result. The results for the Central Aleutians suggest that the slab density may be slightly lower than the value used in our models, but the discrepancy is much less than found for the Tonga-Kermadec model and appears only at long (> 1000 km) wavelengths. Time-dependent flow models incorporating localized region of low viscosity above the wedge which also evolve in time are needed to investigate the implications of these results on the dynamic evolution the thermal structure within the slab-wedge system.

References

Geoffrey A. Abers. Three-dimensional inversion of regional P and A arrival times in the East Aleutians and sources of subduction zone gravity highs. *Journal of Geophysical Research*, 99:4395–4412, 1994.

L. Astiz, T. Lay, and H. Kanamori. Large intermediate depth earthquakes and the subduction process. *Physics of Earth and Planetary Interiors*, 53:80–166, 1988.

Clement G. Chase. Extension behind island arcs and motions relative to hot spots. *Journal of Geophysical Research*, 83:5385–5387, 1978.

A. K. Cooper, D. W. Scholl, and M. S. Marlow. Plate tectonic model of the evolution of the Bering Sea Basin. *Geological Society of America Bulletin*, 87:1119–1126, 1976.

Kazuya Fujita and Hiroo Kanamori. Double seismic zones and stresses of intermediate depth earthquakes. *Geophysical Journal International*, 66:131–156, 1981.

GEBCO. General bathymetric chart of the oceans, British Oceanographic Data Centre. Computer file, February 1997.

John A. Grow. Crustal and upper mantle structure of the central Aleutian Arc. *Geological Society of America Bulletin*, 84:2169–2192, 1973.

Akira Hasegawa, Dapeng Zhao, Shuichiro Hori, Akira Yamamoto, and Shigeki Horiuchi. Deep structure of the Northeastern Japan Arc and its relationship to seismic and volcanic activity. *Nature*, 352:683–689, August 1991.

G. Hirth and D. L. Kohlstedt. Experimental constraints on the dynamics of the partially molten upper mantle 2. Deformation in the dislocation creep regime. *Journal of Geophysical Research*, 100:15441–15449, 1995.

G. Hirth and D. L. Kohlstedt. Water in the oceanic upper mantle: implications for rheology, melt extraction and the evolution of the lithosphere. *Earth and Planetary Science Letters*, 144:93–108, 1996.

Gregory A. Houseman and David Gubbins. Deformation of subducted oceanic lithosphere. *Geophysical Journal International*, 131:535–551, 1997.

S. Karato. Mapping water content in the upper mantle. In J. Eiler, editor, *Subduction Factory, AGU Monograph*, Washington D. C., in press. American Geophysical Union.

P. B. Kelemen, G. Hirth, N. Shimizu, M. Spiegelman, and H. J. B. Dick. A review of melt migration processes in the adiabatically upwelling mantle beneath spreading ridges. *Philosophical Transactions Royal Society London Annals*, 355:283–318, 1997.

G. Laske and G. Masters. A global digital map of sediment thickness. *EOS Trans. AGU*, 78:F483, 1997.

T. Lay, D. H. Christensen, L. Astiz, and H. Kanamori. Temporal variation of large intraplate earthquakes in coupled subduction zones. *Physics of Earth and Planetary Interiors*, 54:258–312, 1989.

F. G. Lemoine, S. C. Kenyon, J. K. Factor, R. G. Trimmer, N. K. Pavlis, and et al. The Development of the Joint NASA GSFC and NIMA Geopotential Model EGM96. Technical report, NASA Goddard Space Flight Center, Greenbelt, Maryland, 1998.

Dan P. McKenzie. Speculations on the consequences and causes of plate motions. *Geophysical Journal of the Royal Astornomical Society*, 18:1–32, 1969.

S. Mei. *The effect of water on the plastic deformation on olivine and olivine-basalt aggregates*. PhD thesis, University of Minnesota, 1999.

Louis Moresi and Michael Gurnis. Constraints on the lateral strength of slabs from three-dimensional dynamic flow models. *Earth and Planetary Science Letters*, 138: 15–28, 1996.

Louis N. Moresi and V. S. Solomatov. Numerical investigations of two-dimensional convection with extremely large viscosity variations. *Physics of Fluids*, 9:2142–2162, 1995.

J. D. Morris, W. P. Leeman, and F. Tera. The subducted component in island arc lavas: constraints from Be isotopes and B-Be systematics. *Nature*, 344:31–36, 1990.

R. D. Müller, W. R. Roest, J. Y. Royer, L. M. Gahagan, and J. G. Sclater. Digital isochrons of the world's ocean floor. *Journal of Geophysical Research*, 102:3211–3214, 1997.

J. Phipps-Morgan. The generation of a compositional lithosphere by mid-ocean ridge melting and its effect on subsequent off-axis hotspot upwelling and melting. *Earth and Planetary Science Letters*, 146:213–232, 1997.

S. M. Rigden, T. J. Ahrens, and E. M. Stolper. Densities of liquid silicates at high pressures. *Science*, 226:1071–1074, 1984.

E. Roth, D. Wiens, and D. Zhao. An empirical relationship between seismic attenuation and velocity anomalies in the upper mantle. *Geophysical Research Letters*, 27:601–604, 2000.

Max W. Schmidt and Stefano Poli. Experimentally based water budgets for dehydrating slabs and consequences for arc magma generation. *Earth and Planetary Science Letters*, 163:361–379, 1998.

David W. Scholl and Richard H. Herzer. Geology and resource potential of the Southern Tonga Platform. In Joel S. Watkins, Feng Shiqiang, and Kenneth J. McMillen, editors, *Geology and Geophysics of Continental Margins, AAPG Memoir*, volume 53, chapter 9, pages 139–156. The American Association of Petrolem Geologists, 1992.

C. H. Scholz and J. Campos. On the mechanism of seismic coupling and back arc spreading at subduction zones. *Journal of Geophysical Research*, 100:22103–22115, 1995.

William Schroeder. The empirical age-depth relation and depth anomalies in the Pacific Ocean Basin. *Journal of Geophysical Research*, 89:9873–9883, 1984.

Tetsuzo Seno and Yoshiko Yamanaka. Arc stresses determined by slabs: Implications for mechanisms of back-arc spreading. *Geophysical Research Letters*, 25(27):3227–3230, September 1998.

Mark Simons. *Localization of Gravity ond Topography: Constraints on the Tectonics and Mantle Dynamics of Earth and Venus.* PhD thesis, Massachusetts Insititute of Technology, Boston, MA, 1996.

Norman H. Sleep. Stress and flow beneath island arcs. *Geophysical Journal International*, 42:827–857, 1975.

Edward Stolper and Sally Newman. The role of water in the pertogenesis of Mariana trough magmas. *Earth and Planetary Science Letters*, 121:293–325, 1994.

Y. Tatsumi, M. Sakayuma, H. Fukuyama, and I. Kushiro. Generation of arc basalt magmas and thermal structure of the mantle wedge in subduction zones. *Journal of Geophysical Research*, 88:5815–5825, 1983.

M. S. Vassiliou, B. H. Hager, and A. Raefsky. The distribution of earthquakes with depth and stress in subducting slabs. *Journal of Geodynamics*, 1:11–28, 1984.

Dan M. Worrall. *Tectonic history and the Bering Sea and the evolution of Tertiary strike-slip basin of the Bering Shelf.* Geological Society of America, Inc., Boulder, Colo., 1991.

D. Zhao, A. Hasegawa, and S. Horiuchi. Tomographic imaging of P and S wave velocity structure beneath Northeastern Japan. *Journal of Geophysical Research*, 97:19909–19928, 1992.

Shijie Zhong and Michael Gurnis. Role of plates and temperature-dependent viscosity in phase change dynamics. *Journal of Geophysical Research*, 99(B8):15903–15917, August 1994.

Shijie Zhong, Michael Gurnis, and Louis Moresi. Role of faults, nonlinear rheology, and viscosity structure in generating plates from instantaneous mantle flow models. *Journal of Geophysical Research*, 103(B7):15255–15268, July 1998.